High-Impedance Fault Detection Using Discrete Wavelet Transform and Frequency Range and RMS Conversion

T. M. Lai, L. A. Snider, *Senior Member, IEEE*, E. Lo, *Member, IEEE*, and D. Sutanto, *Senior Member, IEEE*

***Abstract*—High-impedance faults (HIFs) are faults which are difficult to detect by overcurrent protection relays. Various pattern recognition techniques have been suggested, including the use of Wavelet Transform [1]. However this method cannot indicate the physical properties of output coefficients using the wavelet transform. In this paper we propose to use the Discrete Wavelet Transform (DWT) as well as frequency range and rms conversion to apply a pattern recognition based detection algorithm for electric distribution high impedance fault detection. The aim is to recognize the converted rms voltage and current values caused by arcs usually associated with HIF. The analysis using Discrete Wavelet Transform (DWT) with the conversion yields measurement voltages and currents which are fed to a classifier for pattern recognition. The classifier is based on the algorithm using nearest neighbor rule approach. It is proposed that this method can function as a decision support software package for HIF identification which could be installed in an alarm system.**

***Index Terms*—High-impedance faults (HIFs), pattern recognition, wavelet transforms.**

I. Introduction

HIGH-IMPEDANCE faults (HIFs) are difficult to detect. When a conductor such as a distribution line makes contact with a poor conductive surface or substance the resulting level of fault current is usually lower than the nominal current of the system at the fault location. Therefore, conventional protection relay system will not be able to detect the HIFs and trip the protection relay. The failure of HIF detection leads to potential hazards to human beings and potential fire hazards [2].

HIFs on electrical transmission and distribution networks involve arcing and/or nonlinear characteristics of fault impedance which cause cyclical pattern and distortion. Therefore, the objective of most detection schemes is to identify special features in patterns of the voltages and currents associated with HIFs. In general identification techniques comprises two basic steps: feature extraction and pattern recognition (classification).

Various feature extractors have been proposed by researchers and protection engineers, based on fractal techniques [3], digital signal processing [4], crest factor [5], wavelet transform in high frequency noise patterns [6], dominant harmonic vectors [7], [8]. The Pattern recognition methods which include expert systems [9], [10], and artificial neural networks (ANN) [11]–[13] are used to classify the fault based on the extracted features. It has also been proposed [14], [15] that HIF earth fault protection is more reliable in a five-wire distribution system. Pattern recognition methods aim at detecting characteristic voltage and current distortions caused by arcing faults.

It is generally recognized [16] that, while each of these techniques have had some success at HIF fault detection, there is still no single method to solve the problem of the HIF identification completely. For example, various frequency ranges have been proposed for feature extraction, however for the higher frequency ranges the instrument transformers may introduce errors. Furthermore, there is a trade-off between the criteria of achieving a high degree of dependability (where the HIF detector consistently detects high impedance faults when they occur) and security (ensuring that the HIF detector does not detect an HIF when there is no HIF). The aim of the research presented in this paper, as with other papers dealing with this subject, is to make a meaningful improvement in HIF detection.

The method proposed in this paper uses digital signal processing, where a novel application of the Discrete Wavelet Transform (DWT) is used for extracting the features of the distorted waveforms caused by HIFs, and the Nearest Neighbor Rule (NNR) is used for fault classification. After capturing the voltage and current waveforms from power system simulations, they are analyzed by DWT. The DWT output coefficients are converted to RMS values in various frequency ranges, which are then fed to a NNR pattern classifier to determine the fault or nonfault situations. The method incorporates the statistical nature of HIFs and fault locations, and only low order harmonics of voltage and current are required. These schemes can also potentially be applied for on-line training and customization using actual field HIF data and can function as a decision support software package for HIF identification which could be installed in an alarm system.

The actual dependability of a proposed fault detection scheme can only be determined through extensive staged fault testing, and security can only be determined after an extended time in service. For the purposes of developing the methods, however, simulation provides a practicable alternative. In our research, three representative distribution systems were simulated in the Matlab environment, and several thousand fault and nonfault contingencies were stochastically applied. Dependability was evaluated through determination of the success rate of recognizing fault cases, and the security was determined through determination of the immunity of the method to confounding from

Manuscript received April 11, 2003; revised September 26, 2003. This work was supported in part by Hong Kong Polytechnic University and in part by the Research Grant Council of Hong Kong under Project PolyU 5109/01E. Paper no. TPWRD-00172-2003.

The authors are with the The Hong Kong Polytechnic University, Hong Kong, China.

Digital Object Identifier 10.1109/TPWRD.2004.837836

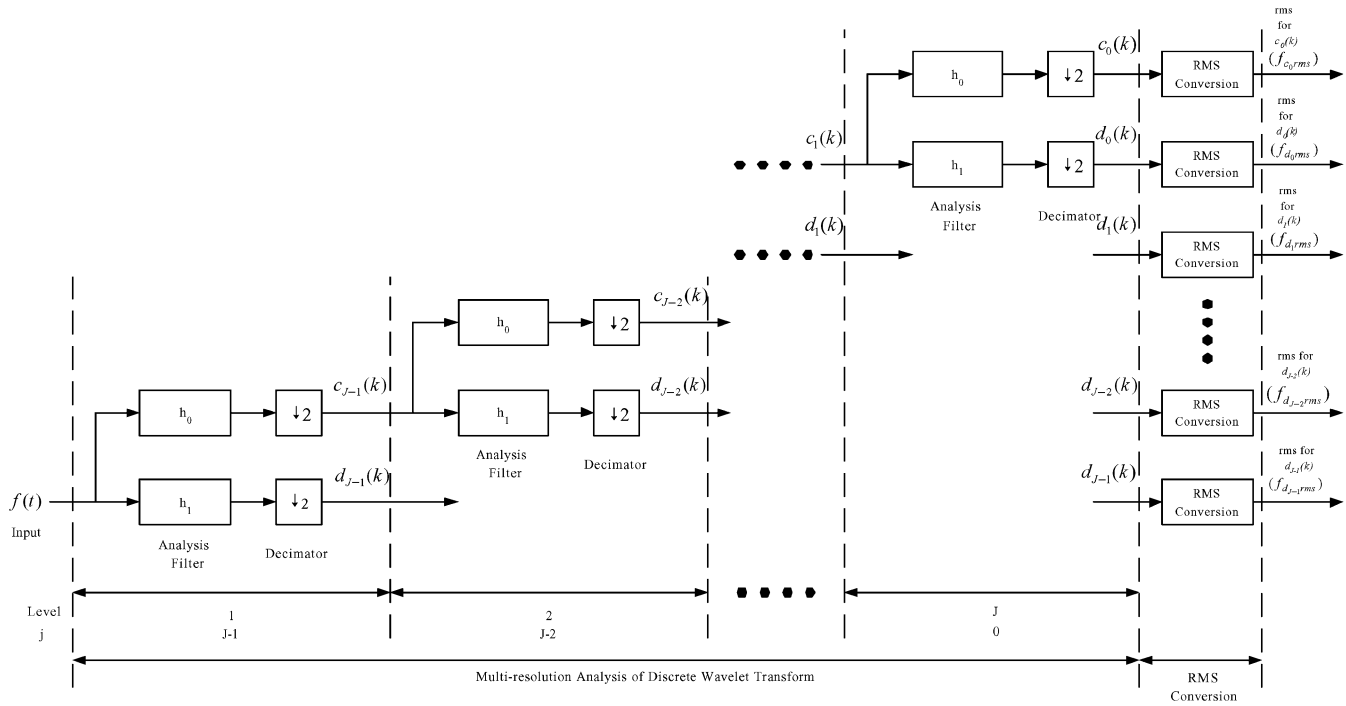

Fig. 1. Schematic diagram of discrete wavelet transform (DWT) and its rms conversion.

contingencies such as capacitor switching as well as linear and nonlinear load switching.

II. Discrete Wavelet Transform (DWT) Model and Multi-Resolution Analysis (MRA)

Wavelet theory and its applications are rapidly developing fields in applied mathematics and signal analysis. The wavelet transform is a tool that divides up data, functions or operators into different frequency components, and then evaluates each component with a resolution matched to its scale [17]. Discrete Wavelet Transform (DWT) resolves the input signal to time, scales, scale coefficients and wavelet coefficients. Multi-resolution analysis (MRA) [18], [19], based on the study of orthonormal, compactly supported wavelet bases, is an extension of DWT and develops representations of a sophisticated signal $f(t)$ in terms of wavelet and scaling functions in different frequency resolution levels.

The schematic diagram of MRA is shown in Fig. 1. The scaling coefficients (approximation) can be computed by taking the inner products of the function $f(t)$ with the scaling basis:

$$c_j(k) = \langle f(t), \phi_{j,k}(t) \rangle = \int_{-\infty}^{\infty} f(t)\phi_{j,k}(t)\,dt. \tag{1}$$

The wavelet coefficients (details) can be computed by taking the inner products of the function $f(t)$ with the wavelet basis:

$$d_j(k) = \langle f(t), \psi_{j,k}(t) \rangle = \int_{-\infty}^{\infty} f(t)\psi_{j,k}(t)\,dt \tag{2}$$

where scale function $\phi_{j,k}(t)$ and wavelet function $\psi_{j,k}(t)$ is determined by the selection of a particular mother wavelet $\psi(t)$ and the following equations.

$$\begin{aligned} \phi_{j,k}(t) &= 2^{j/2}\phi(2^j t - k) \\ \psi_{j,k}(t) &= 2^{j/2}\psi(2^j t - k). \end{aligned} \tag{3}$$

The corresponding relationship of scaling function and wavelet function between two consecutive resolution levels j and $j+1$ are defined in (4) using Mallet algorithm [20] and the lowpass filter h_0 and the highpass filter h_1 can be calculated using Matlab.

$$\begin{aligned} c_j(k) &= \sum_m h_0(m-2k)c_{j+1}(m) \\ d_j(k) &= \sum_m h_1(m-2k)c_{j+1}(m). \end{aligned} \tag{4}$$

One-dimensional wavelet was applied to this power system application. The scales and scale coefficients c and wavelet coefficients d do not reflect the physical properties in the frequency analysis. Consequently, it is difficult to understand and relates the coefficients of the wavelet analysis to measurements. Therefore, the following sections introduce mappings from scale to frequency ranges and from scale coefficients and wavelet coefficients to the rms values of their scale coefficients and wavelet coefficients in each DWT resolution level, respectively.

A. Mapping From Scales to Frequency Ranges

In discrete wavelet transform, a resolution scale is commonly used to represent the degree of resolution. The structure of DWT in MRA is shown in Fig. 1. Two definitions of resolution level

are commonly used: ascending order Level from the finest resolution level (1) to the coarsest resolution level (J) and descending order j from the finest resolution level $(J-1)$ to the coarsest resolution level (0) where J is total resolution level. The relationship between Level and j is defined as follows:

$$\text{Level} = J - j \tag{5}$$

and the resolution levels in terms of Level and j are listed at the bottom of Fig. 1. The resolution scale $\text{scale}_{\text{Level}}$ in each resolution level is defined as:

$$\text{scale}_{\text{Level}} = 2^{J-\text{Level}} = 2^j. \tag{6}$$

In each resolution level, the input signal d_{j+1} in the upper resolution level is split into the approximation c_j by a lowpass filter h_0 and the detail d_j by the highpass filter h_1 in the lower resolution level. Both of output approximation and detail signal are then decimated by 2. Based on the Nyquist theorem (which states that the highest frequency which can be accurately represented is less than one-half of the sampling rate), the maximum frequency of original signal $f(t)$ sampled at $\text{freq}_{f(t)}$ Hz is $\text{freq}_{f(t)}/2$ Hz. The first approximation c_{J-1} and first detail d_{J-1} in resolution level 1 are sampled at half of $\text{freq}_{f(t)}$. Therefore, the maximum frequencies $\text{freq}_{\text{Level}}$ of signals c_j and d_j in each resolution level Level are given in (7):

$$\text{freq}_{\text{Level}} = \frac{\text{freq}_{f(t)}}{2^{\text{Level}}} = \frac{\text{freq}_{f(t)}}{2^{J-j}}. \tag{7}$$

Since the boundary of a lowpass and a highpass filter is half of nyquist frequency, the upper boundary frequency of lowpass filter h_0 and the lower boundary frequency of highpass filter h_1 is the same as half of $\text{freq}_{\text{Level}}$. Therefore, the lower boundary frequency $\text{freq}_{\text{Lower}}$ and upper boundary frequency $\text{freq}_{\text{Upper}}$ of both lowpass filter h_0 and highpass filter h_1 in each resolution level Level are defined as:

$$\begin{aligned}
&\text{freq}_{\text{Lower}} = 0 \\
&\text{freq}_{\text{Upper}} = \frac{\text{freq}_{f(t)}}{2^{\text{Level}+1}} = \frac{\text{freq}_{f(t)}}{2^{J-j+1}} \quad \text{for lowpass filter} \\
&\text{freq}_{\text{Lower}} = \frac{\text{freq}_{f(t)}}{2^{\text{Level}+1}} = \frac{\text{freq}_{f(t)}}{2^{J-j+1}} \quad \text{for highpass filter.} \\
&\text{freq}_{\text{Upper}} = \frac{\text{freq}_{f(t)}}{2^{\text{Level}}} = \frac{\text{freq}_{f(t)}}{2^{J-j}}
\end{aligned} \tag{8, 9}$$

B. Calculation of RMS Values From Scale Coefficients and Wavelet Coefficients

Scale coefficients and wavelet coefficients $\text{coeff}_{\text{signal}}$ and their signal energy E_{signal} representing the distorted signal $f(t)$ at different resolution levels in multi-resolution analysis (MRA) are defined as:

Low Frequency Range

$\Rightarrow$ High Frequency Range

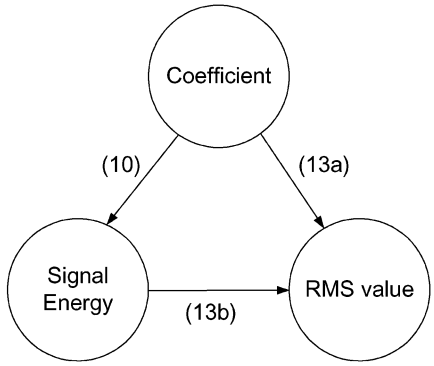

Fig. 2. Relationship of coefficients, signal energy, and rms values.

$$\begin{aligned}
&\text{coeff}_{\text{signal}} = [c_0|d_0|d_1|\ldots|d_{J-2}|d_{J-1}] \\
&E_{c_0} = \|c_0\|_2 = \sqrt{\sum_k |c_0(k)|^2} \\
&E_{d_j} = \|d_j\|_2 = \sqrt{\sum_k |d_j(k)|^2} \\
&E_{\text{signal}} = \left[E_{c_0}|E_{d_0}|E_{d_1}|\ldots\left|E_{d_{J-2}}\right|E_{d_{J-1}}\right] \\
&E_{\text{signal}} = [\|c_0\|_2|\|d_0\|_2|\|d_1\|_2|\ldots|\|d_{J-2}\|_2|\|d_{J-1}\|_2]
\end{aligned} \tag{10}$$

where

J	is total resolution level in this multi-resolution analysis,
c_0 and d_j	are the approximation in level 0 and the detail in level j respectively,
E_{c_0}	is signal energy of the approximation c_0 in level 0,
E_{d_j}	is signal energy of the detail d_j in level j and,
E_{signal}	is signal energy of the scale coefficients and wavelet coefficients $\text{coeff}_{\text{signal}}$.

For the periodic mode of discrete wavelet transform, the rms values of their scale coefficients and wavelet coefficients can be calculated directly from their scale coefficients and wavelet coefficients in their own resolution levels or through their signal energies indirectly. The relationship map is shown in Fig. 2. The conversion equations (11), (12), and (13) are shown as follows and the proof is in Appendix.

The rms values for the details or approximation in each wavelet level can be represented in the periodic-padding (periodic extension at the edges) mode of discrete wavelet transform. For the scale coefficient in level $J(j=0)$, the rms value $f_{c0\text{rms}}$ in level $J(j=0)$ is

$$f_{c_0\text{rms}} = \sqrt{\frac{\|f_{c0}(t)\|_2^2}{L_{f(t)}}} = \sqrt{\frac{\sum_k c_0(k)^2}{2^J L_{c_o}}} \tag{11}$$

where

$L_{f(t)}$	$2^J L_{c_o}$;
$L_{f(t)}$	number of points in $f(t)$;
L_{c_o}	number of points in scale coefficient c_0.

For the wavelet coefficients in each level, the rms values $f_{dj\,\mathrm{rms}}$ in level j are

$$f_{d_j\mathrm{rms}} = \sqrt{\frac{\|f_{dj}(t)\|_2^2}{L_{f(t)}}} = \sqrt{\frac{\sum_k d_j(k)^2}{2^{\mathrm{Level}} L_{d_j}}} = \sqrt{\frac{\sum_k d_j(k)^2}{2^{J-j} L_{d_j}}} \tag{12}$$

where

$L_{f(t)}$ $2^{\mathrm{Level}} L_{d_j} = 2^{J-j} L_{d_j}$

L_{d_j} number of points in wavelet coefficients d_j and

Level is the resolution level in discrete wavelet transform. Therefore, the rms vector $\mathrm{rms}_{\mathrm{signal}}$ calculated from scale coefficients and wavelet coefficients of the distorted signal $f(t)$ at different resolution levels is as follows:

$$\mathrm{rms}_{\mathrm{signal}} = \left[f_{c_0\mathrm{rms}} \middle| f_{d_0\mathrm{rms}} \middle| f_{d_1\mathrm{rms}} \middle| \cdots \middle| f_{d_{J-2}\mathrm{rms}} \middle| f_{d_{J-1}\mathrm{rms}} \right]$$

$$\mathrm{rms}_{\mathrm{signal}} = \left[\sqrt{\frac{\sum_k c_0(k)^2}{2^J L_{c_o}}} \middle| \sqrt{\frac{\sum_k d_0(k)^2}{2^J L_{d_0}}} \middle| \sqrt{\frac{\sum_k d_1(k)^2}{2^{J-1} L_{d_1}}} \middle| \cdots \middle| \sqrt{\frac{\sum_k d_{J-2}(k)^2}{2^2 L_{d_{J-2}}}} \middle| \sqrt{\frac{\sum_k d_{J-1}(k)^2}{2 L_{d_{J-1}}}} \right] \tag{13a}$$

$$\mathrm{rms}_{\mathrm{signal}} = \left[\frac{E_{c_0}}{\sqrt{L_{f(t)}}} \middle| \frac{E_{d_0}}{\sqrt{L_{f(t)}}} \middle| \frac{E_{d_1}}{\sqrt{L_{f(t)}}} \middle| \cdots \middle| \frac{E_{d_{J-2}}}{\sqrt{L_{f(t)}}} \middle| \frac{E_{d_{J-1}}}{\sqrt{L_{f(t)}}} \right] \tag{13b}$$

$$\mathrm{rms}_{\mathrm{signal}} = \left[\frac{\|c_0\|_2}{\sqrt{L_{f(t)}}} \middle| \frac{\|d_0\|_2}{\sqrt{L_{f(t)}}} \middle| \frac{\|d_1\|_2}{\sqrt{L_{f(t)}}} \middle| \cdots \middle| \frac{\|d_{J-2}\|_2}{\sqrt{L_{f(t)}}} \middle| \frac{\|d_{J-1}\|_2}{\sqrt{L_{f(t)}}} \right] \tag{13c}$$

With the above equations, the rms values calculated from scale coefficients and wavelet coefficients in multi-resolution levels can be converted directly from their scale coefficients and wavelet coefficients $\mathrm{coeff}_{\mathrm{signal}}$ or from their signal energy E_{signal}. It is clear from (13b) and (13c) of rms values $\mathrm{rms}_{\mathrm{signal}}$ in terms of their signal energy E_{signal}, that the rms values $\mathrm{rms}_{\mathrm{signal}}$ calculated from their scale coefficients and wavelet coefficients are directly proportional to their signal energy in their resolution levels with a constant $(L_{f(t)})^{-0.5}$.

III. Simulation

A. Simulation Procedures

The simulation comprises three parts: power system model, wavelet transform and pattern recognition model. Fig. 3 shows the flowchart of the simulation. Matlab was used to generate all the system parameters in the fault cases and nonfault cases for the power system simulation according to random fault location and fault situations. The system parameters in fault and nonfault cases were then imported into the power system simulation and the Power System Toolbox was used to determine the targeted voltage and current waveforms of the circuit breaker in the faulted distribution line. These waveforms of voltages and currents in the measurement points on the distribution side of the transformer were then simulated using discrete wavelet transform to analyze the frequency characteristics in various frequency ranges. The rms values of the voltages and currents were calculated using the voltage and current waveforms from the discrete wavelet transform. A classifier was used to recognize the fault cases and nonfault cases using rms values of voltage and current in various frequency bands.

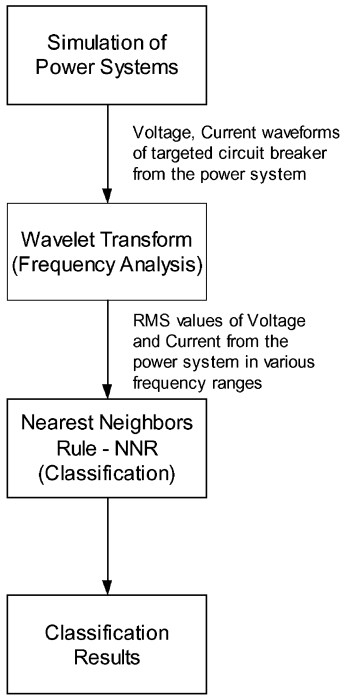

Fig. 3. Simulation model procedures—Matlab application.

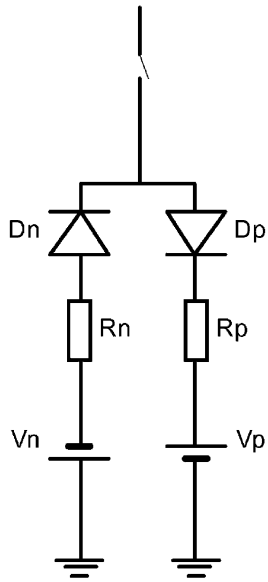

Fig. 4. Simplified two-diode fault model of high-impedance faults.

B. Power System Model—High Impedance Faults (HIFs) and Low Impedance Faults (LIFs) Model

A simplified 2-diode model [21] of HIFs, shown in Fig. 4, was used in the simulation to represent the low frequency phenomena typical of an arcing fault involving sandy soil. The

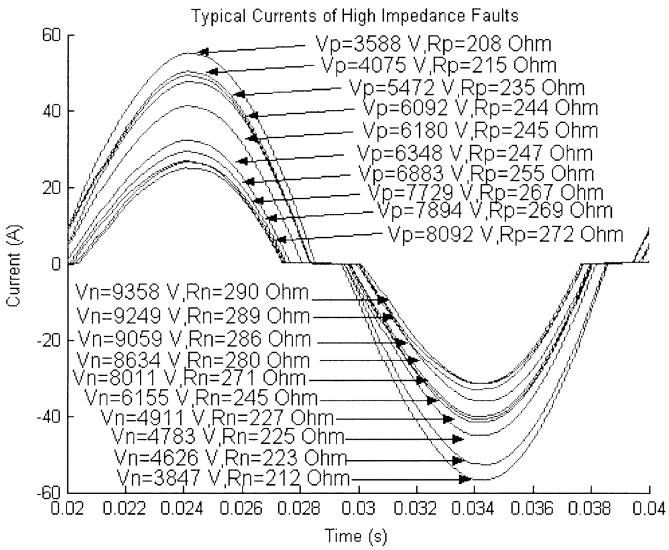

Fig. 5. Typical current of high-impedance faults.

TABLE I
SCALE TO FREQUENCY CONVERSION BASED ON 50 HZ POWER FREQUENCY

Level	Parameter	Frequency Band (Hz)	Harmonics Included
6	$c_{0,k}$	0 – 75	1^{st}
6	$d_{0,k}$	75 – 150	$2^{nd} - 3^{rd}$
5	$d_{1,k}$	150 – 300	$3^{rd} - 6^{th}$
4	$d_{2,k}$	300 - 600	$6^{th} - 12^{th}$
3	$d_{3,k}$	600 - 1200	$12^{th} - 24^{th}$
2	$d_{4,k}$	1200 - 2400	$24^{th} - 48^{th}$
1	$d_{5,k}$	2400 - 4800	$48^{th} - 96^{th}$

model comprises two DC sources, Vp and Vn, which represent the inception voltage of air in soil and/or between trees and the distribution line. The two resistances, Rp and Rn, represent the fault resistance: unequal values allow for asymmetric fault currents to be simulated. When the phase voltage is greater than the positive DC voltage Vp, the fault current flows toward the ground. The fault current reverses when the line voltage is less than the negative DC voltage Vn. For values of the phase voltage between Vn and Vp no fault current flows. The typical fault currents with the HIF model parameters are shown in Fig. 5.

The low impedance fault (LIF) model comprises the appropriate fault resistance switched at the fault location in the distribution line.

C. Implementation of Discrete Wavelet Transform (DWT) Model and Multi-Resolution Analysis (MRA)

In this application, db4 in Daubechies family wavelets was selected for the mother wavelet and the frequency bandwidths of scale and wavelet coefficients of MRA were determined using (8) and (9) shown in Table I after downsampling the input signal $f(t)$ to the sampling frequency of 9600 Hz in order to reduce the computational time.

After the calculation of output voltage and current in various resolution levels from DWT, the rms values $\mathrm{rms}_{\mathrm{signal}}$ of voltages or currents are exported to a classifier.

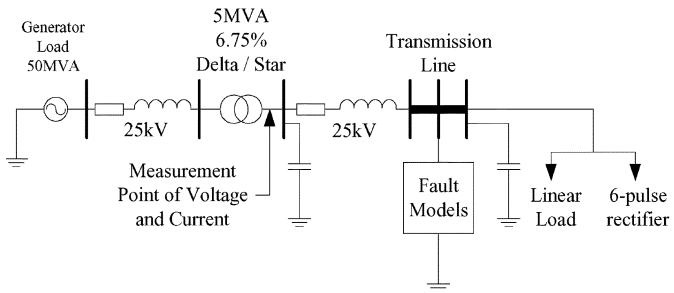

Fig. 6. Schematic diagram of the simulated 25 kV single branch power system network.

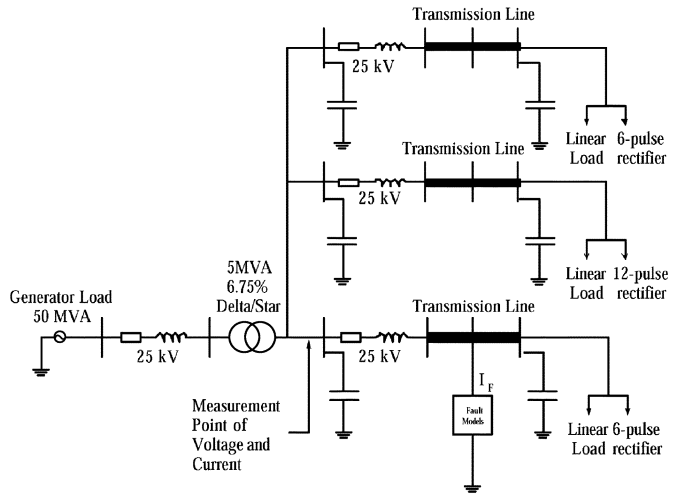

Fig. 7. Schematic diagram of the simulated 25 kV radial power system network.

D. Pattern Recognition

Since normal operation and fault situations do not have specific patterns for their respective distributions, a nonparametric approach in supervised learning was used in this fault classification problem. The nearest neighbor rule (NNR) method [22], [23] is a typical recognition method of the nonparametric approach. It is different from the black-box types of pattern recognition methods, such as neural networks, since NNR can demonstrate the classification results and their decision boundaries between two sorts of data by plotting two-dimensional contour graphs.

The root-mean-square values $\mathrm{rms}_{\mathrm{signal}}$ of voltages and currents in various frequency ranges from the DWT are classified into a training set and a test set respectively. 95% of the rms values were used as a training set to train the decision boundaries using NNR and the rest of the data acted as a test set to validate their decision boundaries.

IV. SYSTEM DESCRIPTION

Three systems studied in this paper are parts of representative 25 kV power distribution networks: i) a distribution network with a single branch of a nonlinear load, ii) a radial distribution network with three branches of nonlinear loads and iii) a meshed network with two sources and various nonlinear loads. Their schematic diagrams are shown in Fig. 6, 7, and 8, respectively.

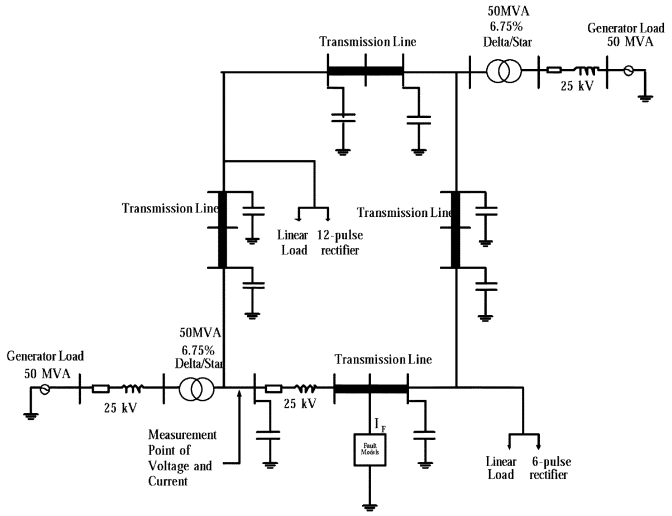

Fig. 8. Schematic diagram of the simulated 25 kV meshed power system network.

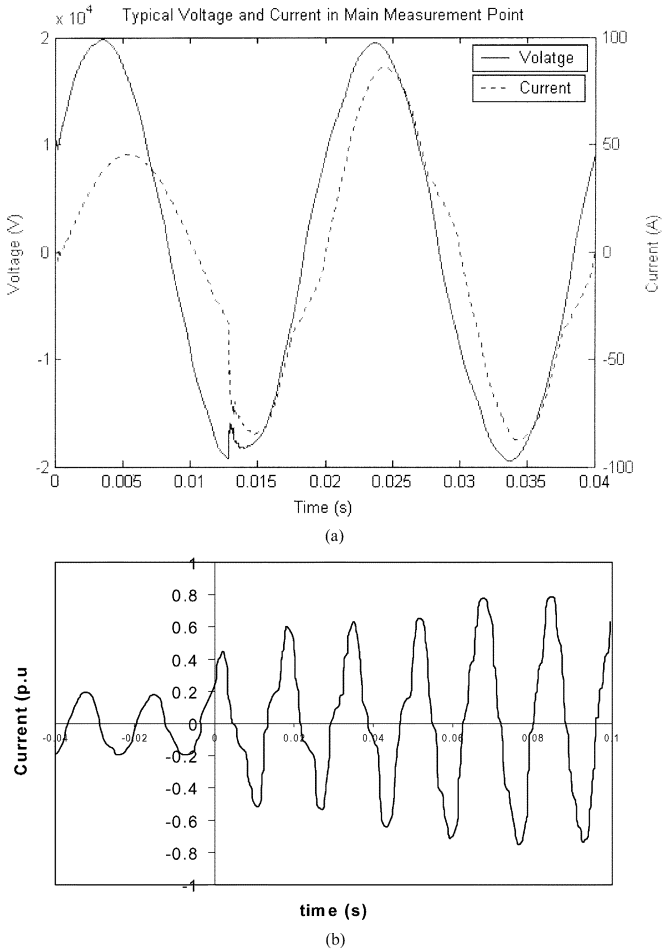

Fig. 9. Simulated waveforms and measured waveform containing high-impedance faults. (a) Simulated waveforms containing high-impedance faults (prefault $t < 0.013$ and postfault $t > 0.013$ s). (b) Measured current waveform containing high-impedance faults (prefault $t < 0$ and postfault $t > 0$ s).

In the single branch distribution network, power is supplied at 25 kV through a 20 km distribution line from a 5 MVA transformer. The network then distributes power to a 4 MVA linear load with power factor 0.8 and a 1 MVA nonlinear load, where a 6 pulse converter is used to represent the nonlinear load. In the radial distribution network with three branches of nonlinear loads, two additional branches, one with a 2 MVA 6-pulse converter load and one with a 4.262 MVA 12-pulse converter load are connected. The meshed network comprises a ring with two 3-phase voltage sources feeding two individual nonlinear loads, one with a 1 MVA 6-pulse converter load and one with a 4.262 MVA 12-pulse converter load. The measurement points for the voltage and current are located at the breaker as shown in the schematic diagrams.

In this paper, 1000 nonfault cases and 1000 fault cases in each system were simulated. The fault cases comprise both high impedance fault model and low impedance fault models. In the simulations, the significant parameters were stochastically selected based on those in real operations. The fault currents were assumed to range from 0.25 to 2 p.u. of overcurrent device settings in the full load situation.

1) Case I—Non-Fault Cases (Normal Operation): In all distribution networks, shunt capacitors banks ranging up to 1 MVAr, linear loads up to their own maximum powers and nonlinear loads up to their own maximum ratings were switched at the sending end and receiving end of the distribution lines. The nonlinear loads comprise three phase 6 pulse converters and 12-pulse converters and the three phase linear loads have their own power factor in accordance with their system configurations. The ratings and breaker closing times of linear loads, nonlinear loads and capacitors were stochastically selected.

2) Case II—Fault Cases: The modeled phase-to-ground HIFs and LIF's with various fault inception angles were simulated at different positions along the faulted distribution lines from the circuit breaker at the source side to distribution loads. Fault location, fault impedance and fault inception angles of both HIFs and LIF's were stochastically selected in the simulation, representing the stochastic variation of soil properties and other characteristics of the HIFs. The ratings of the linear loads and the nonlinear loads, operation schedule in the capacitors at the sending end and receiving end in the distribution lines of the simulated distribution networks were chosen randomly.

V. Simulation Results

A. Comparison of Simulation and Measurement of HIF

The voltage and current waveforms at the sending end of the transmission line of the network shown in Fig. 6 are shown in Fig. 9(a). While field tests for this particular network are not available, it is instructive to make a qualitative comparison with current waveforms corresponding to an HIF fault in a typical distribution network. Such a waveform is shown in Fig. 9(b), which was extracted form [4], and it compares quite well with that of Fig. 9(a).

B. Simulation Results of DWT

The major simulation results of voltage and current in various frequency ranges in phase R at the circuit breaker are shown in Figs. 10 to 14. Correlation scatter plots with decision boundaries

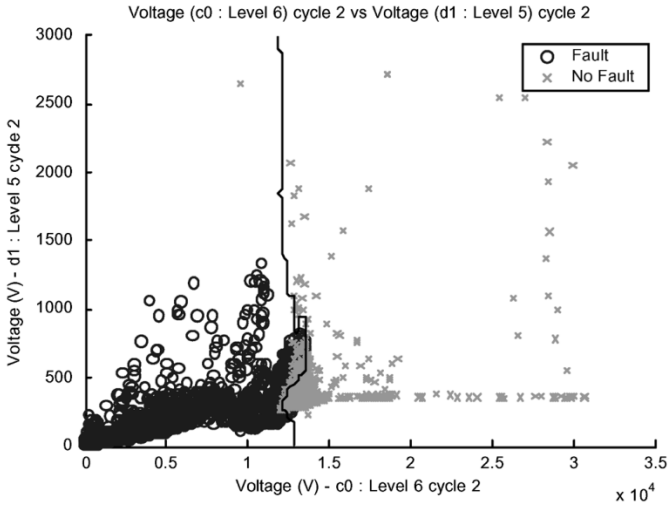

Fig. 10. Voltage (rms from $d_{1,k}$ in Level 5: 150–300 Hz) against Voltage (rms from $c_{0,k}$ in Level 6: 0–75 Hz).

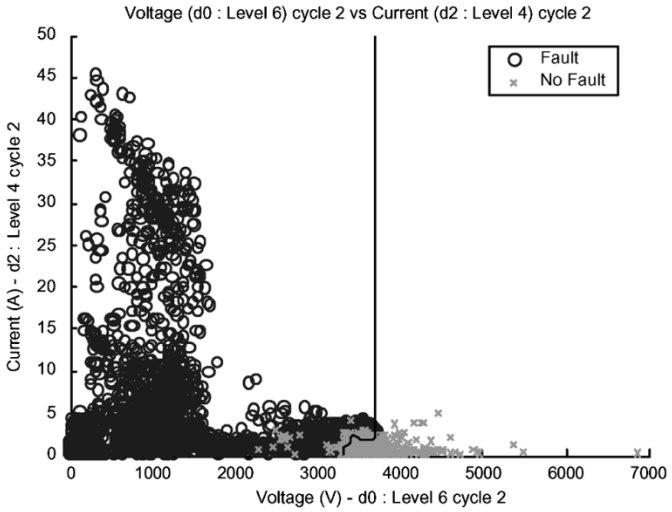

Fig. 11. Current (rms from $d_{2,k}$ in Level 4: 300–600 Hz) against Voltage (rms from $d_{0,k}$ in Level 6: 75–150 Hz).

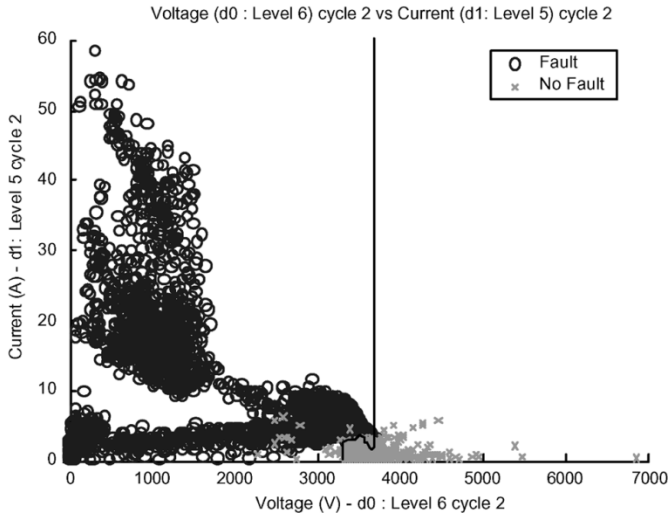

Fig. 12. Current (rms from $d_{1,k}$ in Level 5: 150–300 Hz) against voltage (rms from $d_{0,k}$ in Level 6: 75–150 Hz).

are used to present the correlation of each frequency band of voltage and current components in accordance with Table I.

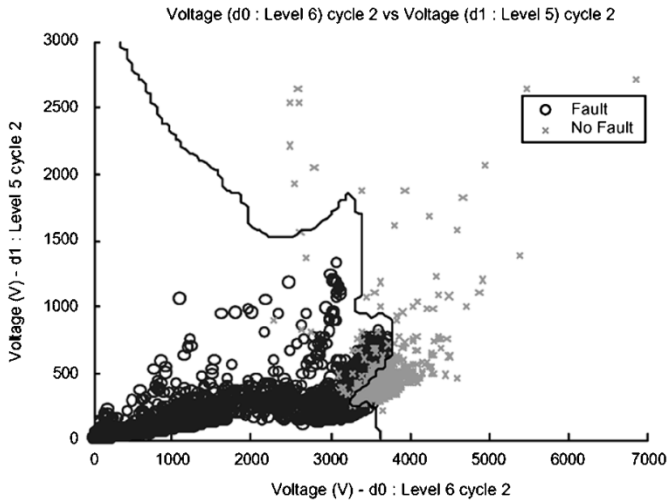

Fig. 13. Voltage (rms from $d_{1,k}$ in Level 5: 150–300 Hz) against Voltage (rms from $d_{0,k}$ in Level 6: 75–150 Hz).

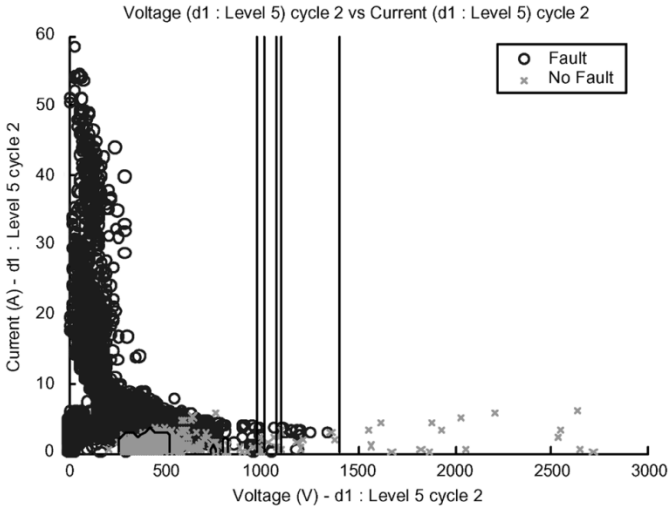

Fig. 14. Current (rms from $d_{1,k}$ in Level 5: 150–300 Hz) against voltage (rms from $d_{1,k}$ in Level 5: 150–300 Hz).

From the simulation results, the rms voltage from $c_{0,k}$ in resolution level 6 (dc to 75 Hz) under normal operation is close to that of the phase voltage source. However, in the fault cases the rms voltage from $c_{0,k}$ between 0 to 75 Hz has a range of approximately zero to 13 kV, as shown in Fig. 10.

The range of voltage in the frequency range between 75 Hz to 150 Hz from $d_{0,k}$ in resolution level 6 is around zero to 3.5 kV, as shown in Figs. 11, 12, and 13. The maximum currents in the frequency range between 150 Hz to 300 Hz from $d_{1,k}$ in resolution level 5 and between 300 Hz to 600 Hz from $d_{2,k}$ in resolution level 4 are 8 A and 5 A respectively in the normal operation and 60 A and 45 A respectively in the fault cases, as shown in Figs. 11, 12, and 14. The maximum currents in the above frequency ranges in the fault cases are 7 to 9 times the magnitude of those in normal operation.

In the pattern recognition, the fault cases and nonfault cases are classified into the training set and test set in the simulation. In the pattern recognitions lower probability errors mean higher successful rates to classify the two above cases. The ranges of errors in the training set in various correlated wavelet levels are

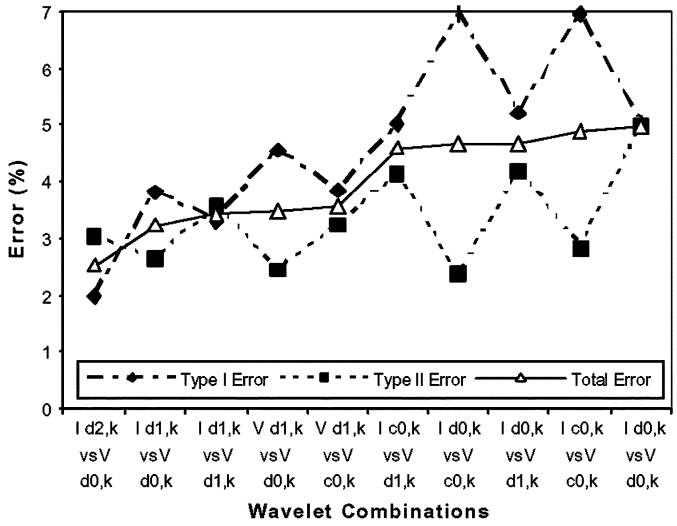

Fig. 15. Type I, II, and total error of different wavelet combinations.

between 2.59% and 45.41%. The errors corresponding to rms values of voltage wavelet coefficients $(d_{0,k})$ in level 6 are between 2.59% and 16.83%.

For the errors in the test set, the ranges of errors in various corresponding wavelet coefficients are between 1.83% and 45.33%. The errors corresponding to rms values of voltage wavelet coefficients $(d_{0,k})$ in level 6 are also between 1.83% and 16.50. the average overall test error is approximately the same as the overall training error.

The total errors show average errors of each combination of wavelet coefficients. The errors corresponding to rms values of voltage wavelet coefficients $(d_{0,k})$ in level 6 are still approximately between 2.52% and 16.80%. The range of total errors is from 2.52% and 45.4%.

An important observation is that it is sufficient to consider only voltages in the frequency range from 0 to 300 Hz, and currents in the frequency range of 0 to 600 Hz for the detection of high impedance faults. Therefore, voltages and currents with low frequency ranges are major factors to classify the high impedance faults and the common faults.

Dependability and security are the important issues of the HIF fault detection. A high level of dependability occurs when the HIF detector correctly recognizes fault cases on its feeder. A high level of security occurs when the HIF detector does not misclassify the nonfault cases into the fault cases. The dependability and security can be evaluated using type I and II errors, where type I and II errors are the percent of incorrect classification for fault and nonfault cases respectively. Fig. 15 summaries type I, II, and total errors corresponding to different wavelet combinations. For example, the type I, II errors and total error of the combination of current $d_{2,k}$ and voltage $d_{0,k}$ are 2%, 3%, and 2.52%, respectively, and the scatter plot of this combination shows in Fig. 13. Suppose that a lower error for fault cases is required in order to achieve better dependability, the decision boundary of the classifier can be adjusted. However, as expected, this will cause an increase of the classification error for the nonfault cases which reduces the security of the fault detection. As a consequence, the HIF classifiers could be optimized to balance between dependability and security such that the total error of the fault detection is minimized, or a trade-off may be made between dependability and security, depending on the specific application.

VI. Conclusion

This paper presented a study of the fault classification in 25 kV electrical distribution systems based on discrete wavelet transform. The study involved computer simulation of power systems, discrete wavelet transform and NNR classification. The electrical faults including HIFs and common faults are stochastic in nature, and depend on factors such as fault location, fault impedance, fault inception angle, other electrical loads, etc. A stochastic simulation was performed, and the error probabilities of classification between the fault cases and normal operation were determined. The classifier had a high success rate at distinguishing between fault cases and nonfault cases, including switching of capacitor banks and nonlinear loads.

The method presented in this paper overcomes the difficulty of using discrete wavelet transform that the output scale coefficients and wavelet coefficients do not represent any physical properties. Using the relationship among scale coefficients and wavelet coefficients, signal energies and rms values, scale coefficients and wavelet coefficients can be converted to rms values directly or through the calculation of signal energies. Therefore, the clear distribution patterns among various characteristic voltage and current rms values calculated from scale coefficients and wavelet coefficients are demonstrated.

The NNR method performs best as a two-parameter input classifier to provide visual pictures of the analysis related to the identification of HIFs. This is demonstrated by the decision boundaries of the two-dimensional scatter plots. However, especially in the significant overlapping areas of fault cases and normal cases, recognition and analysis by experienced engineers is required. However, the identification algorithm of DWT can be applied to produce a decision support software package for HIF identification which could be installed as an alarm system. For example, the package can be installed in the supervision control and data acquisition system as a plug-in component for high impedance fault identification.

Appendix

A. Proof of (11) to 13

This device of is based on periodic-padding (periodic extension at the edges) mode of Discrete Wavelet Transform,

$$f(t) = f_{c0}(t) + f_{d0}(t) + f_{d2}(t) + \cdots + f_{dJ-1}(t)$$

$$f(t) = \sum_k c_0(k)\phi(t-k) + \sum_k \sum_{j=0}^{J-1} d_j(k) 2^{\frac{j}{2}} \psi(2^j t - k)$$

In multiresolution analysis, a set of nested subspaces V_j and W_j are defined as

$$V_{J-1} \supset V_{J-2} \supset \cdots \supset V_j \supset \cdots \supset V_1 \supset V_0$$

$$V_{j+1} = V_j \oplus W_j$$

$$V_j \cap W_j = \{0\}$$

Therefore, a input signal $f(t)$ can be decomposed into their subset signals $f_{c0}(t)$ and $f_{dj}(t)$ in accordance with the subsets V_0 and W_j respectively as follows [19]:

$$f_{c0}(t) = \sum_k c_0(k)\phi(t-k) \tag{A.1}$$

$$f_{dj}(t) = \sum_k d_j(k)2^{\frac{j}{2}}\psi(2^j t-k) \tag{A.2}$$

where $\phi, \psi \in \Re$.

The rms value $f_{c0\mathrm{rms}}$ in level $J(j=0)$ can be calculated from the scale coefficient in level J as follows:

$$f_{c0}(t) = \sum_k c_0(k)\phi(t-k) \tag{A.1}$$

$$\langle f_{c0}(t), f_{c0}(t)\rangle = \left\langle \sum_k c_0(k)\phi(t-k) \sum_k c_0(k)\phi(t-k) \right\rangle$$

$$\|f_{c0}(t)\|_2^2 = \int_{-\infty}^{\infty} \left(\sum_k c_0(k)\phi(t-k)\right)^2 dt$$

By orthonormal basis of scaling functions with different translations

$$\langle \phi_{j,k}(t), \phi_{j,l}(t)\rangle = \int_{-\infty}^{\infty} \phi_j(t-k)\phi_j(t-l)\,dt = \delta(k-l) = \begin{cases} 0 & k \neq l \\ \text{for all} & \\ 1 & k = l \end{cases}$$

for all integer i, j, k, l where $j \leq i$

$$\|f_{c0}(t)\|_2^2 = \int_{-\infty}^{\infty} \left(\sum_k c_0(k)^2\phi(t-k)^2\right) dt$$

$$\|f_{c0}(t)\|_2^2 = \sum_k c_0(k)^2 \int_{-\infty}^{\infty} \phi(t-k)^2\,dt$$

$$\|f_{c0}(t)\|_2^2 = \sum_k c_0(k)^2 \int_0^T \phi(t-k)^2\,dt$$

By orthonormal basis of scale functions

$$\langle \phi_{j,k}(t), \phi_{i,k}(t)\rangle = \int_0^T \phi_j(t-k)\phi_i(t-k)\,dt = \delta(j-i) = \begin{cases} 0 & j \neq i \\ \text{for all} & \\ 1 & j = i \end{cases}$$

$$\|f_{c0}(t)\|_2^2 = \sum_k c_0(k)^2$$

$$\frac{\|f_{c0}(t)\|_2^2}{L_{f(t)}} = \frac{\sum_k c_0(k)^2}{L_{f(t)}}$$

$$\frac{\|f_{c0}(t)\|_2^2}{L_{f(t)}} = \frac{\sum_k c_0(k)^2}{2^J L_{c_o}}$$

The rms value $f_{c0\mathrm{rms}}$ for the approximation in the resolution level 1 $(j=0)$ in terms of scale coefficient or its own signal energy is defined as

$$f_{c_0\mathrm{rms}} = \sqrt{\frac{\|f_{c0}(t)\|_2^2}{L_{f(t)}}}$$

$$f_{c_0\mathrm{rms}} = \sqrt{\frac{\sum_k c_0(k)^2}{2^J L_{c_o}}} \tag{A.3}$$

$$f_{c_0\mathrm{rms}} = \frac{\|c_0\|_2}{\sqrt{L_{f(t)}}} = \frac{E_{c_0}}{\sqrt{L_{f(t)}}} \tag{A.4}$$

where

$L_{f(t)}$ $2^J L_{c_o}$

$L_{f(t)}$ number of points in $f(t)$ and

L_{c_o} number of points in scale coefficient c_0.

Similarly, the rms value $f_{dj\,\mathrm{rms}}$ in level j can be calculated from the wavelet coefficients in level j as follows:

$$f_{dj}(t) = \sum_k d_j(k)2^{\frac{j}{2}}\psi(2^j t-k) \tag{A.2}$$

$$\langle f_{dj}(t), f_{dj}(t)\rangle = \left\langle \sum_k d_j(k)2^{\frac{j}{2}}\psi(2^j t-k), \sum_k d_j(k)2^{\frac{j}{2}}\psi(2^j t-k) \right\rangle$$

$$\|f_{dj}(t)\|_2^2 = \int_{-\infty}^{\infty} \left(\sum_k d_j(k)2^{\frac{j}{2}}\psi(2^j t-k)\right)^2 dt.$$

By orthonormal basis of wavelet functions with different scales and translation

$$\langle \psi_{j,k}(t), \psi_{i,l}(t)\rangle = \left\langle 2^{\frac{j}{2}}\psi(2^j t-k), 2^{\frac{i}{2}}\psi(2^i t-l)\right\rangle = \int_{-\infty}^{\infty} \left(2^{\frac{j}{2}}\psi(2^j t-k)\right)\left(2^{\frac{i}{2}}\psi(2^i t-l)\right) dt = \delta(j-i)\delta(k-l) = \begin{cases} 0 & j \neq i \text{ or } k \neq l \\ \text{for all} & \\ 1 & j = i \text{ and } k = l \end{cases}$$

$$\|f_{dj}(t)\|_2^2 = \int_{-\infty}^{\infty} \left(\sum_k d_j(k)^2 \left(2^{\frac{j}{2}}\psi(2^j t-k)\right)^2\right) dt$$

$$\|f_{dj}(t)\|_2^2 = \sum_k d_j(k)^2 \int_{-\infty}^{\infty} \left(2^{\frac{j}{2}}\psi(2^j t-k)\right)^2 dt$$

$$\|f_{dj}(t)\|_2^2 = \sum_k d_j(k)^2 \int_0^T \left(2^{\frac{j}{2}}\psi(2^j t-k)\right)^2 dt$$

By orthonormal basis of wavelet functions

$$\|f_{dj}(t)\|_2^2 = \sum_k d_j(k)^2$$

$$\frac{\|f_{dj}(t)\|_2^2}{L_{f(t)}} = \frac{\sum_k d_j(k)^2}{L_{f(t)}}$$

$$\frac{\|f_{dj}(t)\|_2^2}{L_{f(t)}} = \frac{\sum_k d_j(k)^2}{2^{\mathrm{Level}} L_{d_j}}.$$

The rms value $f_{dj\,\mathrm{rms}}$ for the detail in the resolution level j in terms of wavelet coefficients or their own signal energies is defined as

$$f_{d_j\mathrm{rms}} = \sqrt{\frac{\|f_{dj}(t)\|_2^2}{L_{f(t)}}}$$

$$f_{d_j\mathrm{rms}} = \sqrt{\frac{\sum_k d_j(k)^2}{2^{\mathrm{Level}}L_{d_j}}} \tag{A.5}$$

$$f_{d_j\mathrm{rms}} = \sqrt{\frac{\sum_k d_j(k)^2}{2^{J-j}L_{d_j}}}$$

$$f_{d_j\mathrm{rms}} = \frac{\|d_j\|_2}{\sqrt{L_{f(t)}}} = \frac{E_{d_j}}{\sqrt{L_{f(t)}}} \tag{A.6}$$

where

$L_{f(t)}$ $2^{\mathrm{Level}}L_{d_j} = 2^{J-j}L_{d_j}$
Level $J-j$
L_{d_j} number of points in wavelet coefficients d_j and

Level is the resolution level in discrete wavelet transform. By (A.3) to (A.6), the rms vector $\mathrm{rms}_{\mathrm{signal}}$ respected to scale coefficients and wavelet coefficients of the distorted signal $f(t)$ at different resolution levels is as follows:

$$\mathrm{rms}_{\mathrm{signal}} = \left[f_{c_0\mathrm{rms}} \middle| f_{d_0\mathrm{rms}} \middle| f_{d_1\mathrm{rms}} \middle| \cdots \middle| f_{d_{J-2}\mathrm{rms}} \middle| f_{d_{J-1}\mathrm{rms}} \right]$$

$$\mathrm{rms}_{\mathrm{signal}} = \left[\sqrt{\frac{\sum_k c_0(k)^2}{2^J L_{c_o}}} \middle| \sqrt{\frac{\sum_k d_0(k)^2}{2^J L_{d_0}}} \middle| \sqrt{\frac{\sum_k d_1(k)^2}{2^{J-1} L_{d_1}}} \middle| \cdots \middle| \sqrt{\frac{\sum_k d_{J-2}(k)^2}{2^2 L_{d_{J-2}}}} \middle| \sqrt{\frac{\sum_k d_{J-1}(k)^2}{2 L_{d_{J-1}}}} \right]$$

$$\mathrm{rms}_{\mathrm{signal}} = \left[\frac{E_{c_0}}{\sqrt{L_{f(t)}}} \middle| \frac{E_{d_0}}{\sqrt{L_{f(t)}}} \middle| \frac{E_{d_1}}{\sqrt{L_{f(t)}}} \middle| \cdots \middle| \frac{E_{d_{J-2}}}{\sqrt{L_{f(t)}}} \middle| \frac{E_{d_{J-1}}}{\sqrt{L_{f(t)}}} \right]$$

$$\mathrm{rms}_{\mathrm{signal}} \left[\frac{\|c_0\|_2}{\sqrt{L_{f(t)}}} \middle| \frac{\|d_0\|_2}{\sqrt{L_{f(t)}}} \middle| \frac{\|d_1\|_2}{\sqrt{L_{f(t)}}} \middle| \cdots \middle| \frac{\|d_{J-2}\|_2}{\sqrt{L_{f(t)}}} \middle| \frac{\|d_{J-1}\|_2}{\sqrt{L_{f(t)}}} \right].$$

REFERENCES

[1] S. J. Huang and C. T. Hsieh, "High-impedance fault detection utilizing a Morlet wavelet transform approach," *IEEE Trans. Power Del.*, vol. 14, no. 4, pp. 1401–1410, Oct. 1999.

[2] Detection of Downed Conductors on Utility Distribution Systems, 1989. IEEE Tutorial Course Text, no. 90EH0310-3-PWR.

[3] B. D. Russell and C. L. Benner, "Analysis of high impedance faults using fractal techniques," *IEEE Trans. Ind. Applicat.*, vol. 33, no. 3, pp. 635–640, May/Jun. 1997.

[4] A. A. Girgas, W. Chang, and E. B. Makram, "Analysis of high-impedance fault generated signals using a Kalman filtering approach," *IEEE Trans. Power Del.*, vol. 5, no. 4, pp. 1714–1724, Oct. 1990.

[5] C. J. Kim and B. D. Russell, "Analysis of distribution disturbances and Arcing faults using the crest factor," *Elect. Power Syst. Res.*, vol. 35, pp. 141–148, 1995.

[6] D. T. W. Chan and X. Yibin, "A novel technique for high impedance fault identification," *IEEE Trans. Power Del.*, vol. 13, no. 3, pp. 738–744, Jul. 1998.

[7] B. M. Aucoin and B. D. Russell, "Detection of distribution high impedance faults using burst noise signals near 60 Hz," *IEEE Trans. Power Del.*, vol. PWRD-2, no. 2, pp. 342–348, Apr. 1987.

[8] D. I. Jeerings and J. R. Linders, "A practical protective relay for down-conductor faults," *IEEE Trans. Power Del.*, vol. 6, no. 2, pp. 565–574, Apr. 1991.

[9] C. J. Kim and B. D. Russell, "Classification of faults and switching events by inductive reasoning and expert system methodology," *IEEE Trans. Power Del.*, vol. 4, no. 3, pp. 1631–1637, Jul. 1989.

[10] B. D. Russell and C. L. Benner, "Arcing fault detection for distribution feeders: Security assessment in long term field trials," *IEEE Trans. Power Del.*, vol. 10, no. 2, pp. 676–683, Apr. 1995.

[11] S. Ebron, D. L. Lubkeman, and M. White, "A neural network approach to the detection of incipient faults on power distribution feeders," *IEEE Trans. Power Del.*, vol. 5, no. 2, pp. 905–914, Apr. 1990.

[12] L. A. Snider and Y. S. Yuen, "The artificial neural networks based relay for the detection of stochastic high impedance faults," *Neurocomput.*, vol. 23, pp. 243–254, 1998.

[13] A. M. Sharaf, L. A. Snider, and K. Debnath, "A neural network based relaying scheme for distribution system high impedance fault detection," in *Proc. 1st New Zealand Int. Two-Stream Conf. Artificial Neural Networks Expert Systems*, 1993, pp. 321–324.

[14] T. A. Short, J. R. Stewart, D. R. Smith, J. O'Brien, and K. Hampton, "Five-wire distribution system demonstration project," *IEEE Trans. Power Del.*, vol. 17, no. 2, pp. 649–654, Apr. 2002.

[15] D. J. Ward, J. F. Buch, T. M. Kulas, and W. J. Ros, "An analysis of the five-wire distribution system," *IEEE Trans. Power Del.*, vol. 18, no. 1, pp. 295–299, Jan. 2003.

[16] J. Tengdin, R. Westfall, and K. Stephan, "High Impedance Fault Detection Technology," PSRC Working Group Members, Rep. PSRC Working Group D15.

[17] I. Daubechies, *Ten Lectures on Wavelets*. Philadelphia, PA: Soc. Industrial Appl. Math., 1992.

[18] G. Strang and T. Nguyen, *Wavelets and Filter Banks*. Cambridge, MA: Wellesley-Cambridge, 1996.

[19] C. S. Burrus, R. A. Gopinath, and H. Guo, *Introduction to Wavelets and Wavelet Transform: A Primer*. Englewood Cliffs, NJ: Prentice-Hall, 1998.

[20] S. G. Mallat, "A theory for multiresolution signal decomposition: The wavelet representation," *IEEE Trans. Pattern Anal. Mach. Intell.*, vol. 11, no. 7, pp. 674–693, Jul. 1989.

[21] A. E. Emanuel, D. Cyganski, J. A. Orr, S. Shiller, and E. M. Gulachenski, "High impedance fault arcing on sandy soil in 15 kV distribution feeders: Contributions to the evaluation of the low frequency spectrum," *IEEE Trans. Power Del.*, vol. 5, no. 2, pp. 676–686, Apr. 1990.

[22] M. Nadler and E. P. Smith, *Pattern Recognition Engineering*. New York: Wiley, 1993.

[23] R. O. Duda, P. E. Hart, and D. G. Stoke, *Pattern Classification*. New York: Wiley, 2001.

T. M. Lai received the B.Sc. degree in Engineering from Hong Kong Polytechnic University in 1996 and the Master's degree in Philosophy from the University of Hong Kong, Hong Kong, China, in 2000. He is currently pursuing the Ph.D. degree in the Department of Electrical Engineering at Hong Kong Polytechnic University.

His research areas include wavelet and artificial intelligence, harmonics, and transient in power systems.

L. A. Snider (M'66–SM'82) was born in Montreal, QC, Canada. He graduated from the Department of Electrical Engineering at McGill University, Montreal, and received the M.Sc. and Ph.D. degrees from the University of Birmingham, Birmingham, U.K.

Currently, he is a Senior Lecturer in the Electrical Engineering Department of the Hong Kong Polytechnic University. He has an extensive background in electric utility research and was one of the founders of the simulation complex of the Hydro Quebec Research Institute, QC, Canada. His interests include real-time power system simulation and high-voltage engineering, and computer applications in teaching.

Edward Lo (M'83) received the B.Sc.(Eng.), M.Phil., and Ph.D. degrees in electrical engineering from the University of Hong Kong, Hong Kong, China, in 1983, 1986, and 1996, respectively.

Currently, he is an Assistant Professor in the Electrical Engineering Department of the Hong Kong Polytechnic University, Hong Kong, China. He has more than 15 years of mixed experience in teaching, research, industry, and consultancy. His research interests include power quality, renewable energy, drives, and traction.

Danny Sutanto (SM'89) received the B.Eng. and Ph.D. degrees from the University of Western Australia, Perth, Australia, in 1978 and 1981, respectively.

Currently, he is a Professor of electrical engineering with the Hong Kong Polytechnic University, Kowloon, Hong Kong. He was also a Power System Analyst with GEC Projects, Sydney, Australia. His main areas of research are power system analysis, power system economics, voltage stability, harmonics, power electronics, and computer-aided education.

Dr. Sutanto is the Executive Committee Member of the Joint Chapter of PES, IAS, and PELS, IEEE HK Section and currently is the IEEE PES Region 10, Regional Representative. He was awarded the Noel Svennson's Award for Teaching Excellence in 1994 with the School of Electrical Engineering at the University of New South Wales, Sydney, Australia.